Clustering analysis of high spatial resolution spectra of asteroid (162173) Ryugu from Hayabusa2/NIRS3

N. Bott, D. Perna, J. D. P. Deshapriya, P. H. Hasselmann, M. A. Barucci, D. L. Domingue, E. Dotto, K. Kitazato, M. Matsuoka, E. Palomba, et al.

Version of Record: https://www.sciencedirect.com/science/article/pii/S0032063322001167
Manuscript_a11057a1538f5ee0b1b37e2c6e43298e

Clustering analysis of high spatial resolution spectra of asteroid (162173) Ryugu from Hayabusa2/NIRS3

N. Bott[1] (nicolas.bott36@gmail.com), D. Perna[1], J. D. P. Deshapriya[1], P. H. Hasselmann[1], M. A. Barucci[2], D. L. Domingue[3], E. Dotto[1], K. Kitazato[4], M. Matsuoka[2], E. Palomba[6], T. Usui[5] and M. Fulchignoni[2]

[1]INAF – Osservatorio Astronomico di Roma, Via Frascati 33, 00078 Monte Porzio Catone, Italy, [2]LESIA, Observatoire de Paris, Université PSL, CNRS, Université de Paris, Sorbonne Université, Meudon, France, [3]Planetary Science Institute, Tucson, AZ, USA, [4]University of Aizu, Fukushima, Japan, [5]Institute of Space and Astronautical Science (ISAS), Japan Aerospace Exploration Agency (JAXA), Sagamihara, Japan, [6]INAF – Istituto di Astrofisica e Planetologia Spaziali, Istituto Nazionale di Astrofisica (INAF), Rome, Italy

Highlights

- We selected high-resolution near-infrared spectra of asteroid Ryugu
- We applied a multivariate statistical analysis at both global and local scale
- Small heterogeneities of composition/alteration are identified
- No clear spatial correlation was found with multispectral images of Ryugu

Abstract

Asteroids, and more globally small bodies, are keys to unravel the origin and the evolution of our Solar system. Remnants of the material which formed planets early on, they captured the composition and the conditions of formation of the latter at that time, since they did not undergo too harsh internal alteration during their lifetimes. The Hayabusa2 spacecraft explored the Cb-type asteroid (162173) Ryugu between June 2018 and November 2019, notably collecting data with its Near-InfraRed Spectrometer (NIRS3) in the 1.8-3.2 μm range. We selected five NIRS3 datasets among the ones having the highest spatial resolution on which we applied the G-mode multivariate statistical analysis, in order to spot small heterogeneities at the surface of Ryugu. Both global scale and local scale cases were investigated. With a confidence level of 3σ, we obtained two classes at global and local scales, while decreasing to 2σ results in the identification of more classes (five at global scale, four at local scale). Overall, our results are consistent among them and with previous studies. In particular, terrains spectrally redder as well as terrains spectrally bluer than the average surface are newly identified by our analysis. The floors of all main craters at the surface of Ryugu appear redder than their surroundings, and are associated with a probable smaller grain size material. A large depression of the Northern hemisphere may contain bluer heterogeneities likely due to a more packed or/and fresher, subsequently deposited material. Finally, a comparison with data from the Hayabusa2 optical camera ONC-T shows no evident correlation between the spectral properties in the near-infrared and in the visible.

Keywords

Near-Earth asteroids; Spectroscopy; Photometry

1. Introduction

The investigation of asteroids is essential to improve our understanding of the history of our Solar system, since most of them did not undergo a harsh thermal alteration or any differentiation. They contain primitive material in various quantities depending on their origin and evolution. The majority of asteroids are concentrated in the Main Belt, but some approach Earth's orbit or even cross it. These are called Near Earth Asteroids (NEAs). NEAs that are particularly big (absolute magnitude H≤22, i.e. about ≥140 m in diameter with an assumed albedo of 14%[1]) and can get very close to Earth (Earth Minimum Orbit Intersection Distance E_{MOID}≤0.05 au) are known as Potentially Hazardous Asteroids (PHAs). NEAs, and especially PHAs, are searched, followed and studied with an increasing dedication to improve our knowledge of the small bodies population and its evolution, but also for planetary defense reasons.

(162173) Ryugu is a Cb spectral type [Kitazato et al., 2019; Sugita et al., 2019], rubble-pile [Watanabe et al., 2019] asteroid, and is a PHA due to its size (r_{eq} = 502 ± 2 m, r_{pol} = 438 ± 2 m [Watanabe et al., 2019], H = 19.39 [2]) and its close encounters to Earth (Earth MOID = 0.001 AU, i.e. 0.389 lunar distance[3]). It was the target of the JAXA Hayabusa2 space mission [Watanabe et al., 2017], whose spacecraft co-orbited the Sun with the asteroid in close proximity between June 2018 and November 2019. Two touchdown operations (TD1 on February 22nd 2019, TD2 on July 11th 2019) were successfully completed to sample Ryugu's surface in different locations, one of them after having dropped the Small Carry-on Impactor (SCI) to reveal the fresher material underneath the top layer of the surface. These samples were returned to Earth in December 2020 and are currently being analysed [Pilorget et al.,

[1] https://cneos.jpl.nasa.gov/about/neo_groups.html
[2] https://minorplanetcenter.net/iau/ECS/MPCArchive/2022/MPO_20220112.pdf
[3] https://ssd.jpl.nasa.gov/

2021; Tachibana et al., 2022; Yada et al., 2021]. In particular, preliminary analyses of these returned samples showed Ryugu and CI meteorites are close in terms of mineralogical and oxygen isotopic compositions (e.g., [Yada et al., 2021; Young et al., 2022]). Hayabusa2 also acquired remote sensing data thanks to five onboard instruments, including the Optical Navigation Camera - Telescope (ONC-T) [Kameda et al., 2017; Suzuki et al., 2018], which mapped Ryugu's surface in seven different colors and the Near InfraRed Spectrometer (NIRS3) [Iwata et al., 2017], a point-spectrometer which collected spectra in the 1.8-3.2 µm spectral range with a complete coverage of the surface.

Ryugu has an overall uniformly dark (reflectance factor of 0.017 ± 0.002 at 2.0 µm [Kitazato et al., 2019]), slightly red-sloped and hydrated surface, characterised by the presence of a weak, narrow absorption band at 2.72 µm attributed to Mg-phyllosilicates [Kitazato et al., 2019]. Recent studies using independent methods of analyses identified minor heterogeneities of composition on Ryugu's surface. [Barucci et al., 2019] analysed ONC-T data from July 12th 2018 and NIRS3 data from July 11th and 19th and October 30th 2018 using the G-mode multivariate statistical tool (see Section 2.2) and found several small regions slightly different mainly in terms of spectral slope, both in the visible and near-infrared. Slight variations of the 2.72 µm band were also observed. These regions were interpreted as containing different amounts of phyllosilicates, as being more or less fresh due to various exposure to space weathering, or having different grain sizes than the rest of the surface. [Matsuoka et al., 2020] applied a statistical method combining various techniques (K-means clustering, Principal Component Analysis, Independent Component Analysis) on NIRS3 data from July 11th 2018, and also suggested grain size variations to explain the spectral reddening.

In this study, we pursue and complement the above analyses using the same method as in [Barucci et al., 2019], but with datasets at higher spatial resolution and/or better coverage. In section 2, we describe these datasets and we remind the main points of the method. Then in

section 3, we present the results we obtained and we discuss them. In section 4 we expose a comparison with ONC-T data, and we end with some conclusions and perspectives in section 5.

2. Data and methods

2.1. Selection and correction of data

We selected five NIRS3 datasets available at the JAXA Data Archives and Transmission System[4] to ensure a global coverage of the surface of Ryugu while improving the used spatial resolution where possible. Information about these datasets are summarized in Table 1, and their respective coverage are displayed in Figure 1.

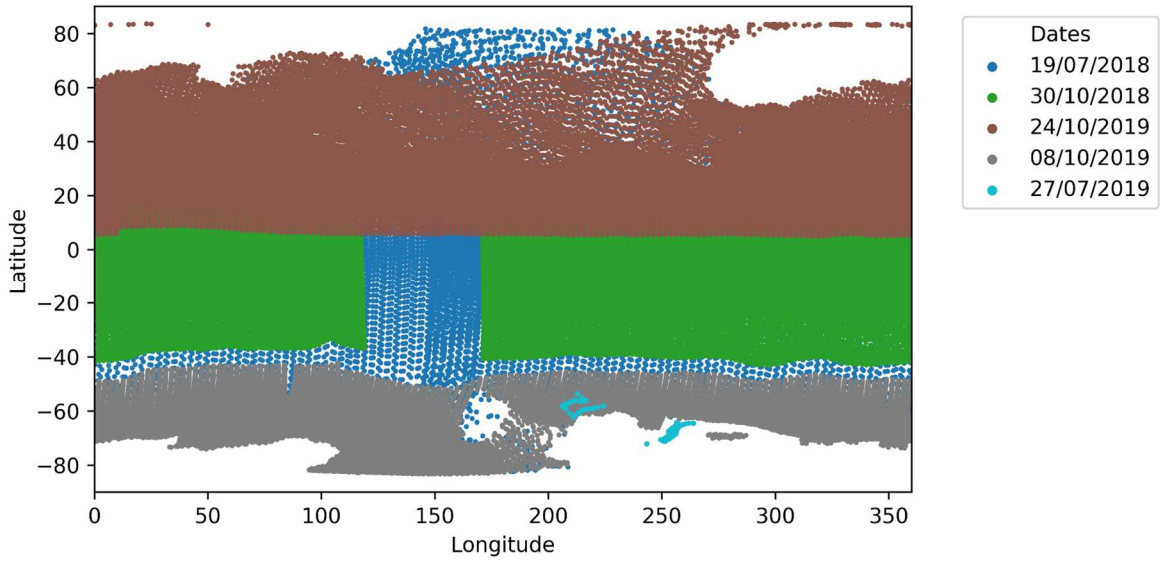

Figure 1. Coverage of each dataset selected for this study

[4] https://hayabusa2.darts.isas.jaxa.jp/nirs3/

Date of acquisition	Total # of spectra	Latitude range (°)	Longitude range (°)	Spatial resolution range (m per footprint)*	Phase angle range (°)	Incidence angle range (°)	Coverage description
2018-07-19	13,230	-83.0–81.7	0–360	18.2–22.2	17.5–18.6	5.0–70.0	Global
2018-10-30	17,282	-43.0–21.3	0–360	9.4–10.5	7.7–8.3	2.2–66.0	Equatorial region
2019-07-27	105	-71.3–-56.0	210.6–264.0	11.6–11.9	38.8–39.4	37.5–69.7	South pole
2019-10-08	11,696	-83.1–-42.2	0–360	13.2–14.4	19.5–20.0	2.8–70.0	Southern hemisphere
2019-10-24	16,314	5.0–73.6	0–360	7.7–9.7	32.7–33.4	10.8–70.0	Northern hemisphere

* before standardization of spectra

Table 1. General information about the five datasets selected for this study.

All data have been thermally corrected [Kitazato et al., 2019], photometrically corrected and standardized to common illumination and viewing conditions (incidence angle = 30°, emission angle = 0°, phase angle = 30°). Only the observations for which incidence and emission angles are lower than 70° were considered for this correction. More details on the approach and methodology for the photometric correction can be found in [Matsuoka et al., (in prep.)].

ONC-T data were considered subsequently for comparison with our results with NIRS3 data. We used the normal albedo maps of Ryugu from [Yokota et al., 2021]. They consist of an image cube of the whole surface of Ryugu (99.4% coverage) within the seven broadband filters of ONC-T (*ul* = 397.5 nm; *b* = 479.8 nm; *v* = 548.9 nm, *n* = 589.9 nm; *w* = 700.1 nm; *x* = 857.3 nm; and *p* = 945.1 nm). For further details on the data, see [Yokota et al., 2021].

2.2. The G-mode statistical analysis

To analyze the data described above, we used a multivariate statistical tool called G-mode, adapted from the original code from [Coradini et al., 1977; Fulchignoni et al., 2000; Gavrishin et al., 1992] by [Hasselmann et al., 2013]. Among its initial usages, this method enabled to establish asteroid taxonomies (e.g. [Barucci et al., 1987]) and transneptunian taxonomy [Barucci et al., 2005]. It was applied more recently to spacecraft-based spectro-photometric data of planetary surfaces, such as those of Phoebe [Tosi et al., 2005], the nucleus of comet 67P/Churyumov-Gerasimenko [Perna et al., 2017b], and asteroids Ryugu [Barucci et al., 2019] and Bennu [Barucci et al., 2020].

From an input sample of N observations (here the number of spectra), each expressed by M variables (here the reflectance at selected wavelengths) with their respective uncertainties, the G-mode identifies unimodal distributions in the sample and assigns consequently each observation to an homogeneous group, characterized by its spectral properties. The statistical weight of each variable is also computed. There is no other intervention from the user than

the choice of the confidence level. This parameter, labeled q, is expressed in terms of σ (for example, a 3σ confidence level corresponds to a 99.7% probability of assigning a spectrum into the correct group). The lower the q, the more detailed the classification, but also the higher the risk of misclassifying an observation.

2.3. Definition of spectral parameters

Several spectral parameters have been used to characterize the spectral properties of the G-mode classification we obtained. We defined three spectral parameters for the NIRS3 data:

1. The first parameter is the spectral slope (in %/100 nm), i.e. the slope of the spectrum considered in the 2.18-2.63 µm spectral range.
2. The second parameter is the band depth (in %), i.e. the depth of the 2.72 µm band of the spectrum. This depth is calculated using a linear fitting at both band edges at 2.68 and 2.77 µm, then removing the continuum and using the formula $d = 1 - r_N$, where d is the band depth and r_N the normalized reflectance at 2.72 µm.
3. The third parameter is the reflectance at 2.05 µm, i.e. the closest wavelength to 2.0 µm, which was used to determine the reflectance factor of Ryugu [Kitazato et al., 2019].

In addition, we selected four spectral parameters for the ONC-T data:

1. The reflectance *b* band (479.8 nm)
2. The reflectance *v* band (548.9 nm)
3. The reflectance *x* band (857.3 nm)
4. The ratio between the reflectance at *x* and *b* bands

All the spectral parameters described above were used only after the G-mode was applied on the data, to better characterize the spectral properties of each class and improve the analysis. Thus, the spectral parameters were not used as inputs for the G-mode analysis itself.

3. Analyses at global and local scales

We applied the G-mode on the reflectance values at 24 relevant wavelengths among the 128 available channels of NIRS3, for each of the selected dataset described in Section 2.1. These wavelengths have been previously chosen to consider the part of the spectrum with the best signal-to-noise ratio [Barucci et al., 2019], and they are reported in Table A.1. (see Appendix A.). These individual analyses produced very consistent classifications for close values of q (see Table 2). Hence, we decided to merge all the datasets into a single dataset, whose spatial resolution map is presented in Figure 2.

Date of acquisition	2018-07-19	2018-10-30	2019-10-08	2019-10-24
Confidence level to obtain 4 classes	2.2	2.0	2.0	2.0

Table 2. Values of the confidence level *q* leading to 4 classes for each NIRS3 dataset.

N.B. No classification could be obtained when applying the G-mode on the dataset of 2019-07-27, probably due to its very small size.

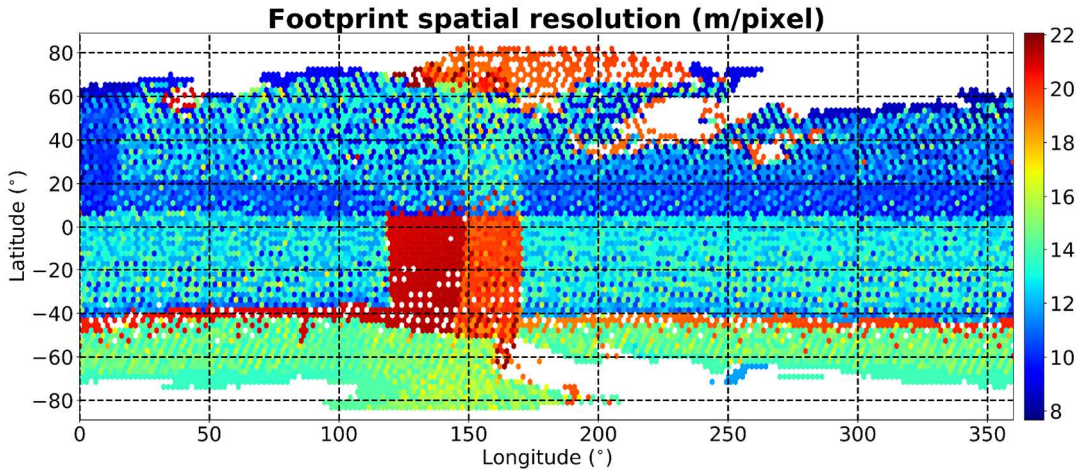

Figure 2. Spatial resolution of the data selected for this study.

Statistical weights of the variables driving the classification are shown in Figure 3. The detailed values are given in Table A.1. (see Appendix A.). In each case described hereafter, they are fairly equally distributed for wavelengths longward of 2.4 µm.

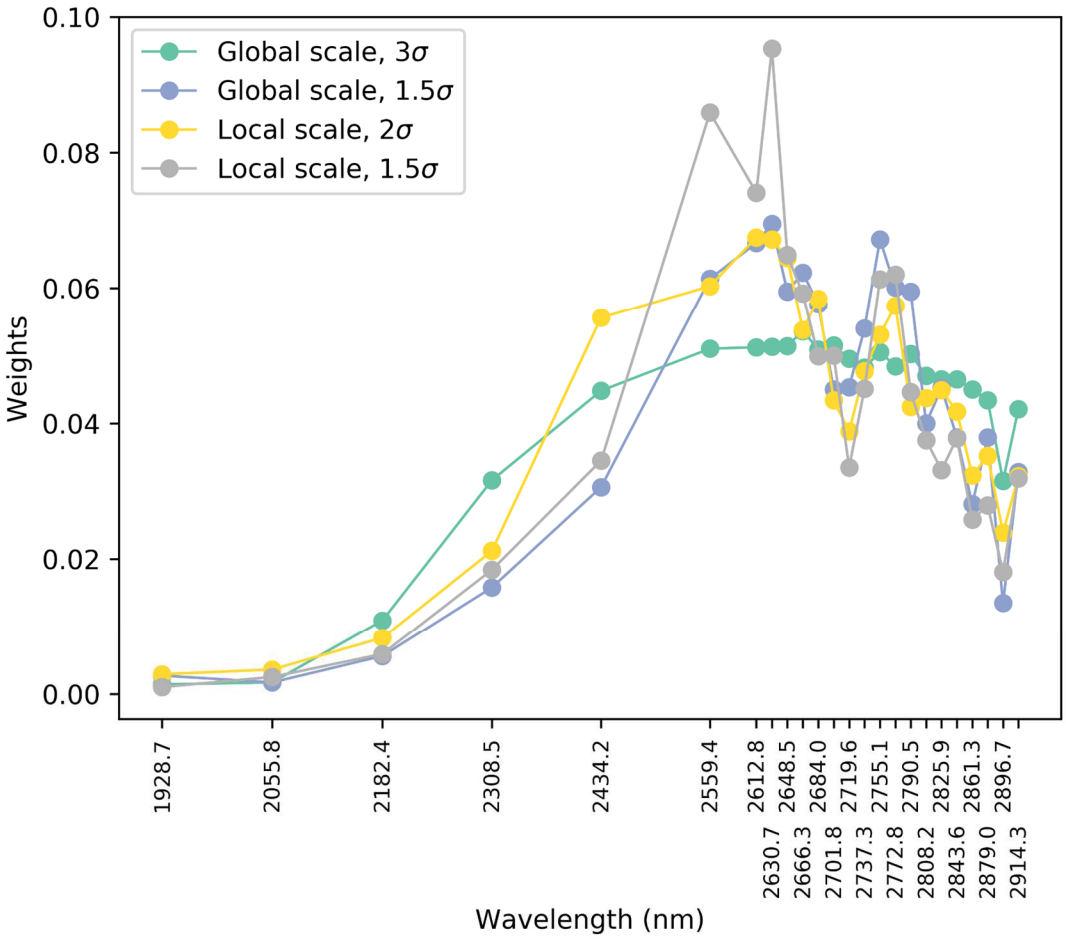

Figure 3. Statistical weights of the 24 parameters (i.e. the reflectance at the 24 selected wavelengths) for the four G-mode classification described in the following sections.

3.1. Global scale: Analysis of merged datasets

With a confidence level of 3σ, we obtain two classes (see Figure 4.a.). Class 1 contains the majority (99.0%) of the spectra in the merged sample, thus corresponding to the average spectral properties of Ryugu at global scale. Class 2 has spectra redder than the ones of class 1. The band depth variation does not seem to be statistically significant.

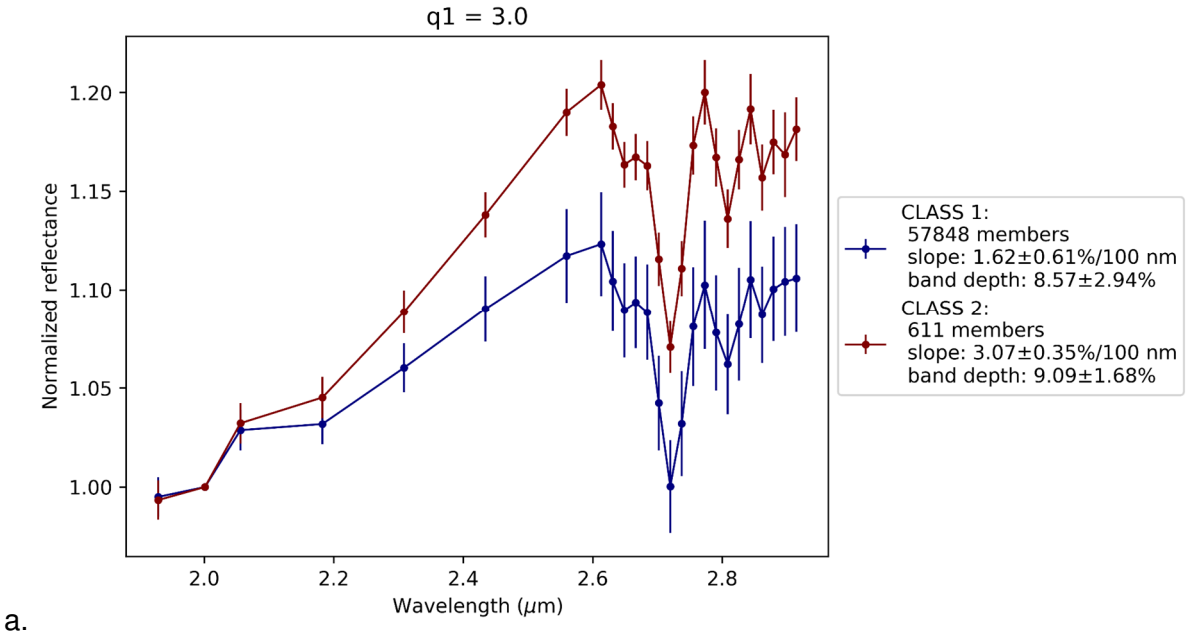

a.

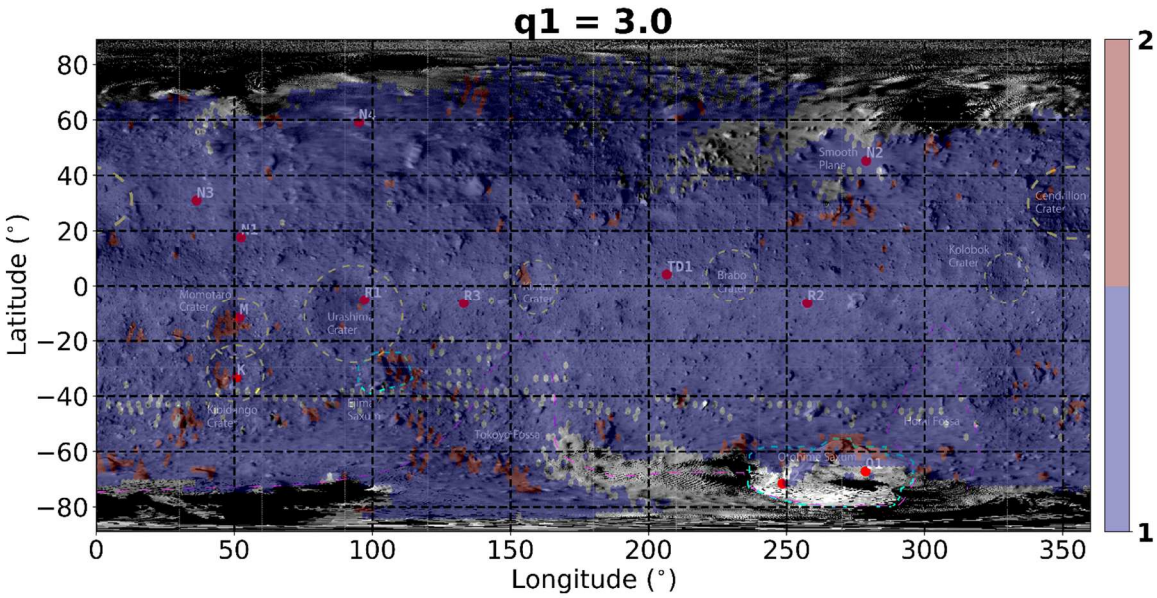

b.

Figure 4. a. Mean spectra of each G-mode class obtained with a confidence level of 3σ on the merged dataset sample.

b. Geographic distribution of each G-mode class at the surface of Ryugu ($q = 3\sigma$). Background global image from [Tatsumi et al., 2020a].

The geographic distribution of these two classes on Ryugu (see Figure 4.b.) shows that class 2 is concentrated inside some craters (Momotaro and Kibidango in particular), on some

boulders in the Southern hemisphere between longitude 0° and 100°, in Ejima Saxum, Otohime Saxum and Tokoyo Fossa, and finally to the South of a large depression in the Northern hemisphere, centered at ~50°N, 260°E, and hosting smooth plains. We note our results are in very good agreement with those obtained by [Barucci et al., 2019].

When decreasing the confidence level down to 1.5σ, five classes are identified in the merged sample (see Figure 5.a.). Again, class 1 includes most of the spectra (86.0%) and can be attributed to the average properties of Ryugu. Classes 2 to 4 have redder spectra than class 1, while class 5 contains bluer spectra. The band depth variation is also not significant from a statistical point of view.

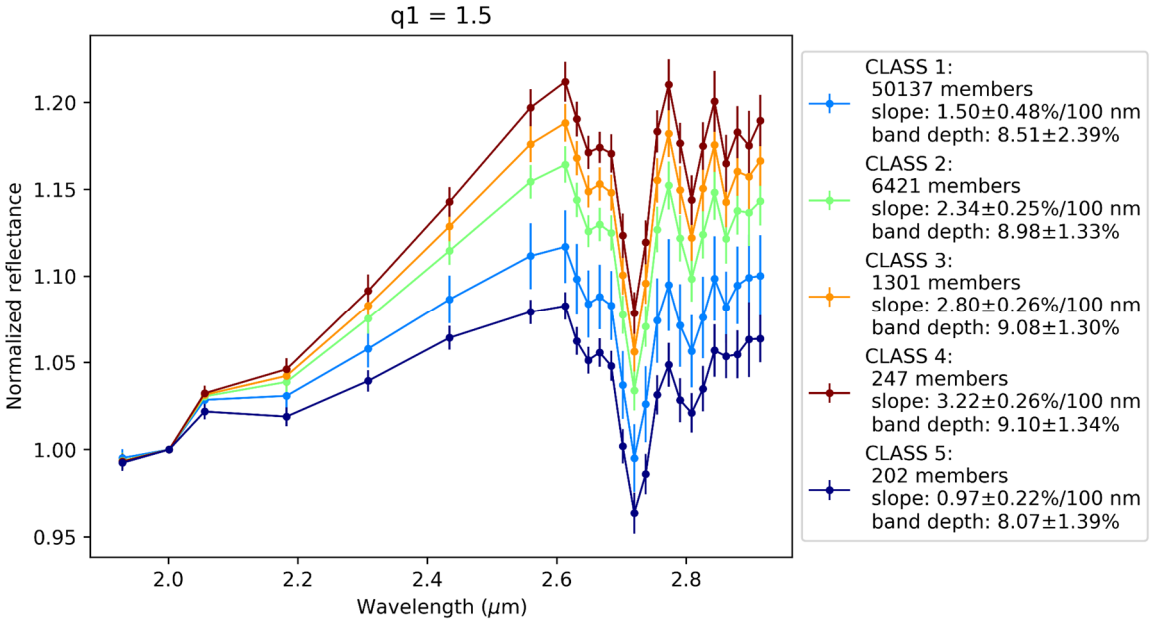

a.

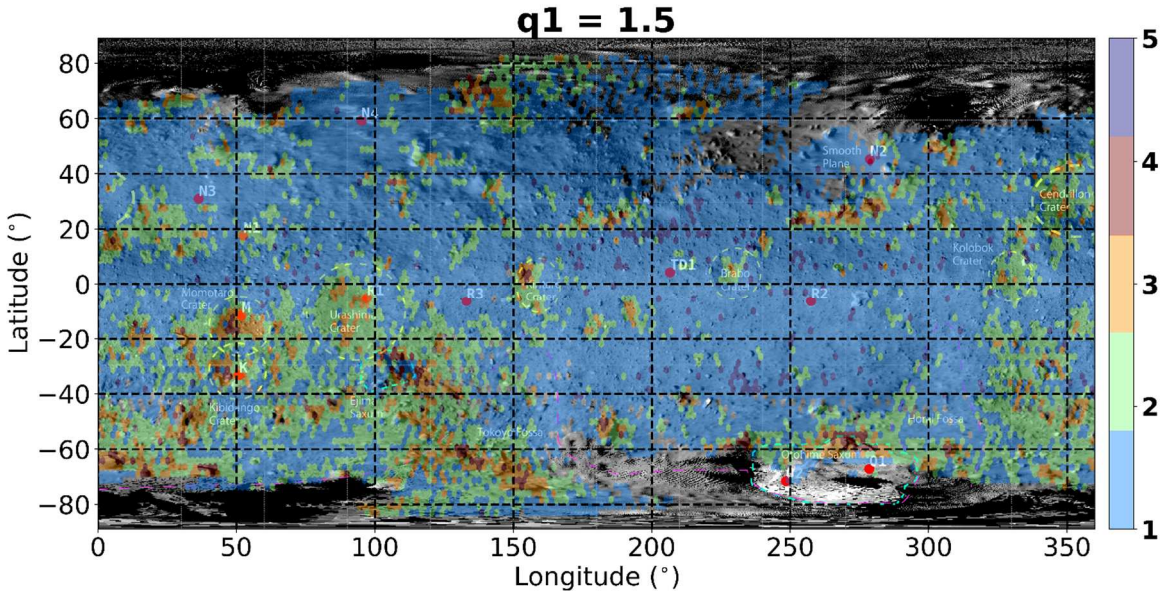

b.

Figure 5. a. Mean spectra of each G-mode class obtained with a confidence level of 1.5σ on the merged dataset sample.

b. Geographic distribution of each G-mode class at the surface of Ryugu (q = 1.5σ). Background global image from [Tatsumi et al., 2020a].

At the surface of Ryugu (see Figure 5.b.), classes 2 to 4 have a geographic distribution similar to class 2 for q = 3σ, but more widespread and in additional locations (e.g. inside Urashima, Kintaro, Brabo, Kolobok and Cendrillon craters; to the East of Cendrillon crater; to the South of Kolobok crater). Class 5 is more sparse on the surface than classes 2 to 4, but seems restricted to low- to middle-latitudes, mainly to the West and the South of the large depression of the Northern hemisphere. These observations for q = 1.5σ are also in very good agreement with the results for q = 2σ of [Barucci et al., 2019].

The results presented above are not influenced by geometric effects. No clear correlation has been found between the G-mode classifications and the incidence and emission angles of data (see Appendix B.), which implies the quality of the photometric correction.

3.2. Local scale: Analysis of the large depression

Based on the above analysis, the large depression of the Northern hemisphere appears naturally as a region of interest. Thus, we used the dataset of October 24th 2019 and its better spatial resolution to investigate it further. We selected only the region delimited by 20-60°N and 230-300°E, resulting in the selection of 1279 spectra.

The confidence level had to be decreased more than in the previous cases, yet keeping an acceptable probability of misclassification. Thus, for $q = 2.0\sigma$, two classes are identified by the Gmode G-mode (see Figure 6.a.). Class 1 contains most of the spectra of the sample (86.5%), and can be attributed to the global spectral properties of Ryugu. Class 2 includes redder spectra, with a non-significant difference in band depth between the two classes.

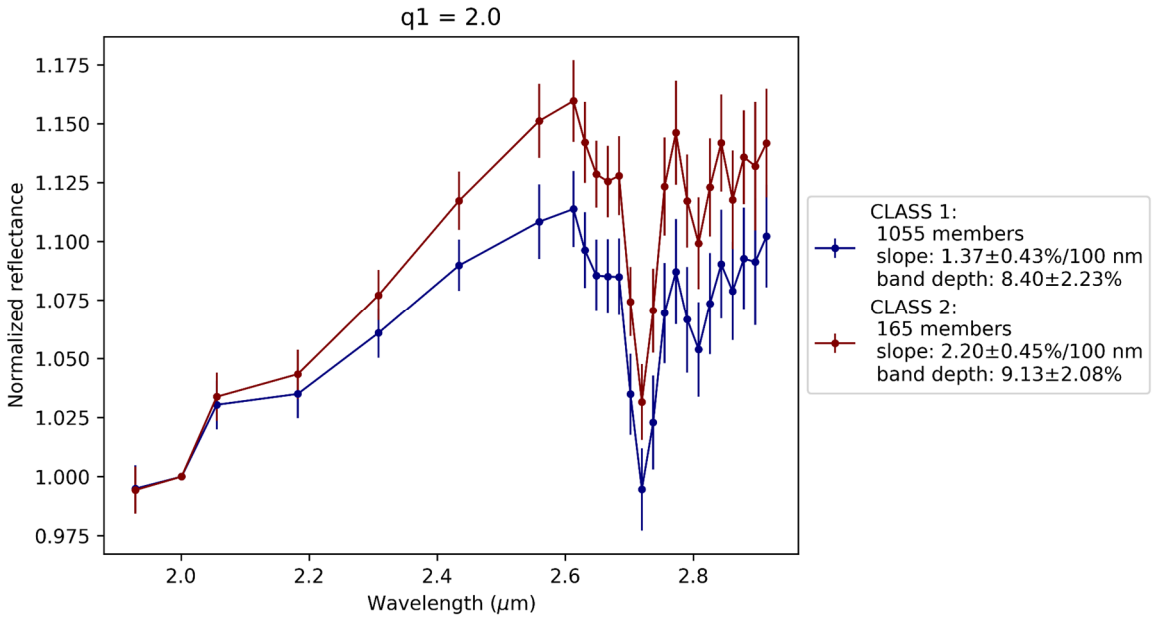

a.

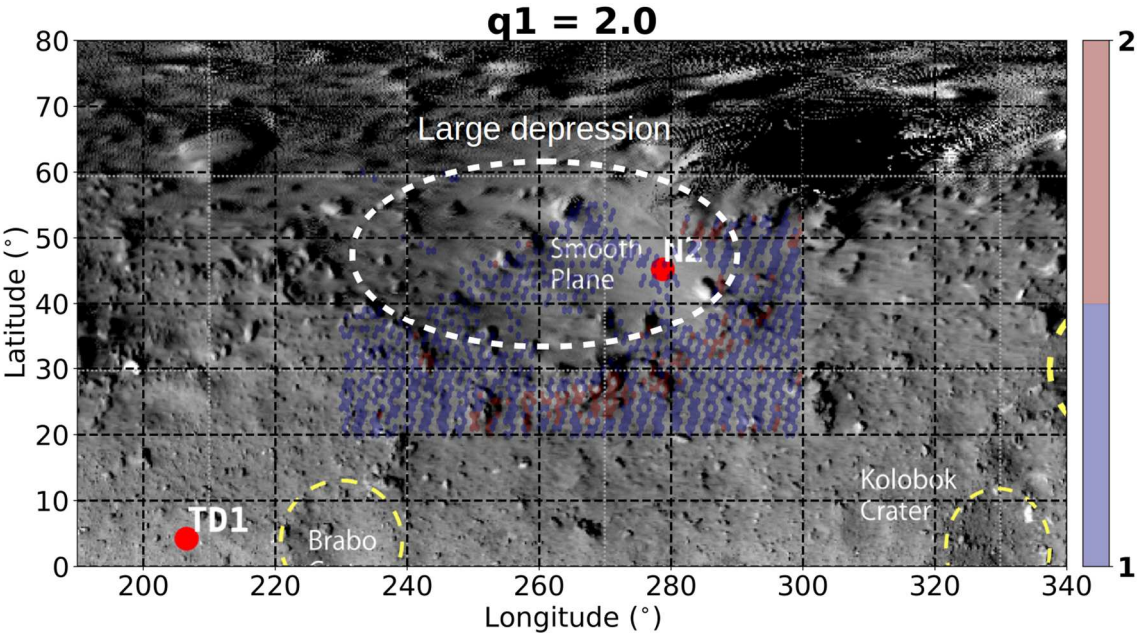

b.

Figure 6. a. Mean spectra of each G-mode class obtained with a confidence level of 2.0σ on the 2019-10-24 dataset restricted to the large depression area.

b. Geographic distribution of each G-mode class at the surface of Ryugu (q = 2.0σ). The background map is centered on the large depression. Background global image from [Tatsumi et al., 2020a].

Figure 6.b. shows the geographic distribution of both classes at the surface of Ryugu. Class 2 is clearly concentrated around the large depression, from its South to its East near surroundings. The distribution is very close to the one obtained with the merged dataset for q = 3.0σ (see Figure 4.b.).

By lowering the confidence level down to 1.5σ, we obtain four classes (see Figure 7.a.). Again, class 1 includes a large part of the spectra of the sample (74.8%), thus corresponding to the average spectral properties of Ryugu. Classes 2 and 4 have redder spectra than class 1, while class 3 includes the bluest spectra. The band depth variation is not statistically significant.

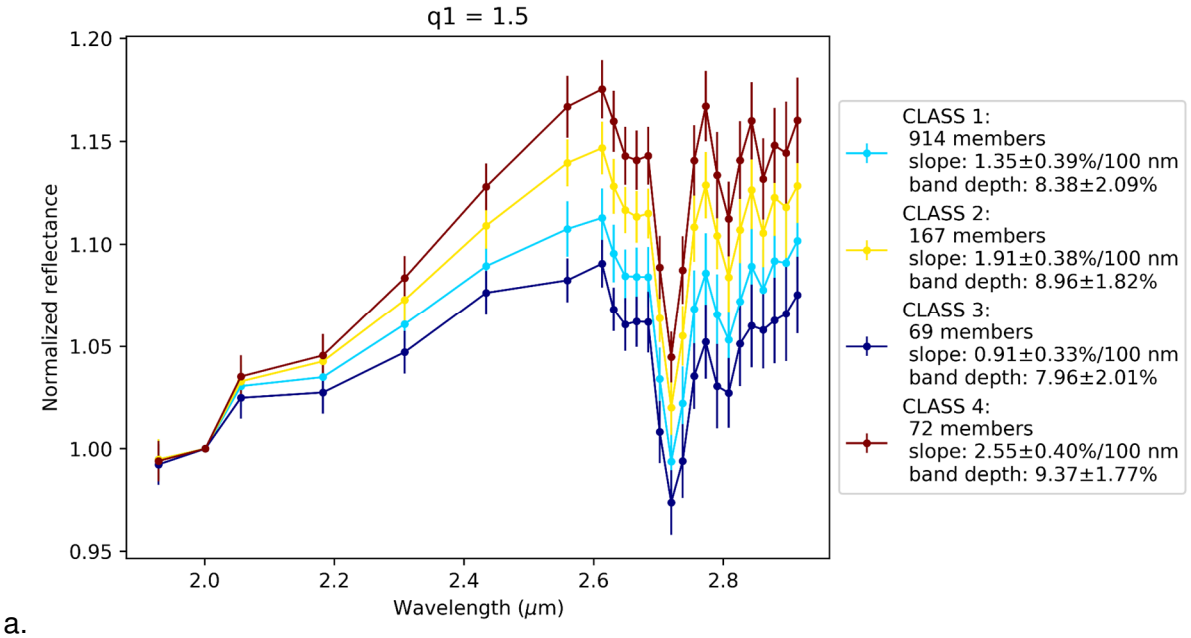

a.

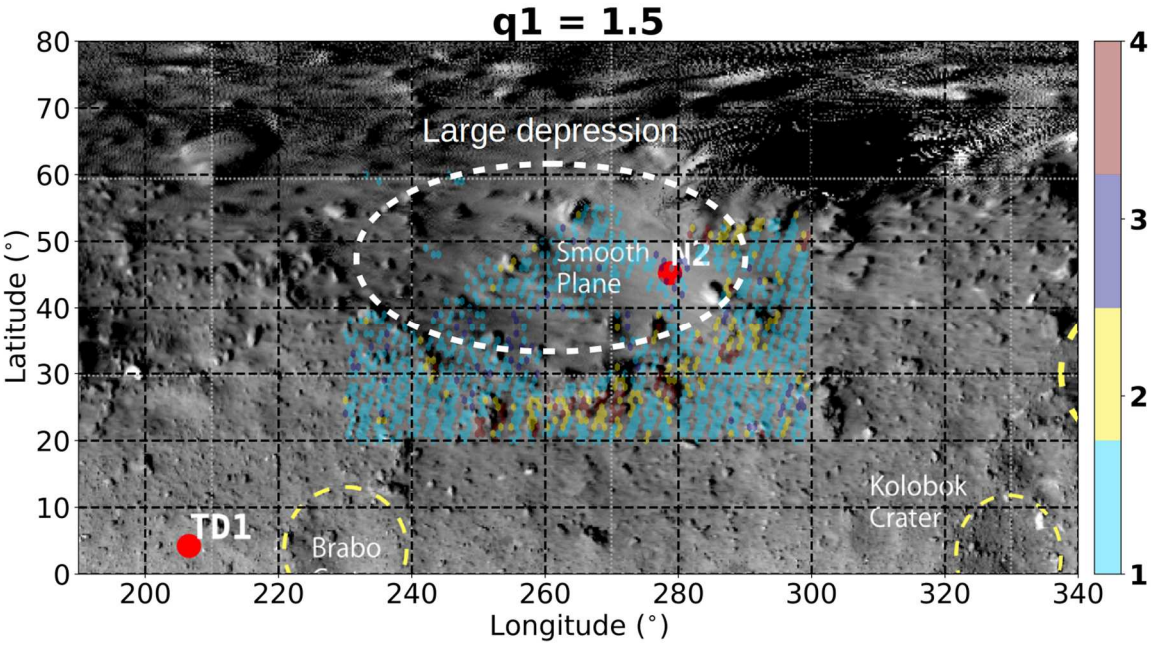

b.

Figure 7. a. Mean spectra of each G-mode class obtained with a confidence level of 1.5σ on the 2019-10-24 dataset restricted to the large depression area.

b. Geographic distribution of each G-mode class at the surface of Ryugu (q = 1.5σ). The background map is centered on the large depression.Background global image from [Tatsumi et al., 2020a].

At the surface of Ryugu (see Figure 7.b.), classes 2 and 4 are clearly distributed close to each other, i.e. from the South to the East surroundings of the large depression, similarly to the case for $q = 2.0\sigma$ (see Figure 6.b.). Class 3 is mainly located in the smooth plains inside the large depression, but also in small areas to its West (~35°N, 235°E) and to its East (~25°N, 295°E). This time, although the confidence levels are the same ($q = 1.5\sigma$), the geographic distributions in this area vary slightly between the merged dataset (see Figure 5.b.) and the dataset restricted to the large depression. This is due to a different number of classes, which can be explained by the difference in size of both datasets. However, the geographic distribution presented in Figure 7.b. is in good agreement with the one obtained by applying the G-mode to the dataset from 2019-10-24 alone.

3.3. Discussion: properties of the surface at both scales

At both global and local scales, we obtained a similar trend, with two classes at higher values of the confidence level and more classes (five at global scale, four at local scale) when decreasing q. At the scale of the large depression of the Northern hemisphere, however, the confidence level had to be smaller (2σ, i.e. ~95.4% probability of right classification instead of 3σ, i.e. ~99.7% probability) to obtain two classes as at global scale (see Section 3.2 and in particular Figure 6). This can be a combined effect of the smaller size of the sample and of a greater homogeneity of the dataset. The results obtained at both scales confirm the high homogeneity of the surface of Ryugu as reported in previous studies [Barucci et al., 2019; Kitazato et al., 2019], even though potential bluer heterogeneities (class 3) in the smooth plains of the large depression are spotted only at local scale. It is interesting to mention that the geographic distribution we obtained at global scale (see Figure 5.b.) is also in good agreement with the results of [Matsuoka et al., 2020]. They used an independent statistical method to classify NIRS3 spectra, and they highlighted the spectral properties of the equatorial region of Ryugu. This shows the robustness of both approaches.

An interesting observation is that the main craters labeled at the surface of Ryugu (Momotaro, Kibidango, Urashima, Kintaro, Brabo, Kolobok and Cendrillon) all have a redder floor than their surroundings, except for the large depression in the Northern hemisphere (see Figure 5). On the mosaic image of Ryugu from [Tatsumi et al., 2020a], the material inside the large depression appears brighter and is labeled as 'smooth plains', implying that it may be composed of finer regolith than elsewhere on the surface. Besides, both G-mode classifications (at global and at local scales, see Figures 5 and 7) show the interior of the large depression may contain heterogeneities spectrally bluer (class 5) than the average properties of Ryugu (class 1). Yet, [Domingue et al., 2021] importantly reminded that the presence, even in small quantities (5%), of fine grains in a sample containing coarse grains turns its spectral slope from blue to red [Binzel et al., 2015; Cloutis et al., 2018]. Thus, grain size alone cannot explain the spectral properties of the smooth plains of the large depression. On the contrary, packing can account for these properties. Indeed, based on the work of [Lantz et al., 2017], unpacked powder of carbonaceous meteorites is redder and darker than the pellet (packed powder) of the same material. Therefore, a direct impact could have produced the large depression, packing the regolith present there to form the smooth plains. Yet, the latter hypothesis is difficult to support at the moment, since no formation process of this depression has been proposed up to now. On the other hand, the presence of fresher/less weathered material may play an important role. [Lantz et al., 2017] showed that low albedo, carbonaceous chondrites tend to brighten and bluen when undergoing ion irradiation, which simulates solar wind irradiation of primitive asteroids like Ryugu. Carbonization processes such as hydrogen loss and carbon structural changes were suggested to explain these spectral effects. Also, [Tatsumi et al., 2021] recently justified the bluer character of both poles of Ryugu by low temperature and low solar-wind implantation conditions experienced by these regions. Besides, [Watanabe et al., 2019] produced a geopotential map showing a slight, but distinguishable minimum where the large depression is located, while the boulder and the bright area to the North correspond to a maximum. Thus, a nearby impact (but not necessarily

at the exact location of the depression) could have lifted fresher regolith from the latter regions, and which could have deposited at the closest geopotential minimum, i.e. inside the large depression.

4. Comparison with ONC-T data

We also compared the properties of NIRS3 spectra of each G-mode class with their respective counterparts in ONC-T data to see how they spatially correlate. Each NIRS3 spectrum was associated with a pixel of the normal albedo map of Ryugu from [Yokota et al., 2021] by minimizing the distance between the center of the NIRS3 spectrum footprint and the pixels of the map. We computed the spectral parameters for NIRS3 and ONC-T data as described in Section 2.3: the near-infrared spectral slope, the 2.72 µm band depth and the reflectance at 2.05 µm for NIRS3 spectra; the reflectance values at *b* (479.8 nm), *v* (548.9 nm) and *x* (857.3 nm) bands, and the ratio between the reflectance at *x* and *b* bands. Finally, we extracted the median values and the median absolute deviation for each G-mode class. The results at global scale are summarized in Table 3.

b band	Class 1	Class 2	Class 3	Class 4	Class 5
NIR spectral slope (%/100 nm)	1.3850 ± 0.3073	2.3516 ± 0.1903	2.8086 ± 0.1828	3.1523 ± 0.2326	0.9838 ± 0.1687
2.72 µm band depth (%)	8.4755 ± 0.8977	8.9402 ± 0.7808	9.0560 ± 0.7565	9.0239 ± 0.8799	8.1252 ± 0.9687
Reflectance at 2.05 µm	0.01678 ± 0.00125	0.01697 ± 0.00109	0.01712 ± 0.00129	0.01759 ± 0.00140	0.01622 ± 0.00102

Reflectance at b band	0.04235 ± 0.00248	0.04226 ± 0.00238	0.04246 ± 0.00214	0.04266 ± 0.00200	0.04196 ± 0.00316

v band	Class 1	Class 2	Class 3	Class 4	Class 5
NIR spectral slope (%/100 nm)	1.3858 ± 0.3105	2.3440 ± 0.1890	2.8103 ± 0.1846	3.1788 ± 0.2262	0.9838 ± 0.1675
2.72 µm band depth (%)	8.4727 ± 0.8994	8.9406 ± 0.7750	9.0472 ± 0.7687	9.0375 ± 0.8497	8.1284 ± 0.9567
Reflectance at 2.05 µm	0.01679 ± 0.00125	0.01700 ± 0.00110	0.01707 ± 0.00129	0.01753 ± 0.00144	0.01623 ± 0.00105
Reflectance at v band	0.04204 ± 0.00137	0.04209 ± 0.00181	0.04203 ± 0.00141	0.04213 ± 0.00128	0.04216 ± 0.00178

x band	Class 1	Class 2	Class 3	Class 4	Class 5
NIR spectral slope (%/100 nm)	1.3836 ± 0.3067	2.3476 ± 0.1914	2.8104 ± 0.1844	3.1523 ± 0.2304	0.9844 ± 0.1679
2.72 µm band depth (%)	8.4707 ± 0.9026	8.9439 ± 0.7811	9.0713 ± 0.7644	8.9997 ± 0.8694	8.1268 ± 0.9621
Reflectance at 2.05 µm	0.01679 ± 0.00126	0.01697 ± 0.00110	0.01714 ± 0.00128	0.01759 ± 0.00139	0.01623 ± 0.00104
Reflectance at x band	0.04176 ± 0.00082	0.04167 ± 0.00083	0.04168 ± 0.00079	0.04168 ± 0.00068	0.04158 ± 0.00101

x/b-band ratio	Class 1	Class 2	Class 3	Class 4	Class 5

NIR spectral slope (%/100 nm)	1.3832 ± 0.3077	2.3481 ± 0.1908	2.8095 ± 0.1842	3.1487 ± 0.2335	0.9838 ± 0.1692
2.72 µm band depth (%)	8.4735 ± 0.9005	8.9433 ± 0.7829	9.0692 ± 0.7576	9.0103 ± 0.8803	8.1268 ± 0.9597
Reflectance at 2.05 µm	0.01679 ± 0.00126	0.01698 ± 0.00110	0.01717 ± 0.00129	0.01770 ± 0.00140	0.01622 ± 0.00103
x band/b band ratio	0.9860 ± 0.0610	0.9879 ± 0.0488	0.9871 ± 0.0425	0.9854 ± 0.0468	0.9825 ± 0.0845

Table 3. Median values of each parameter for each G-mode class obtained with the merged dataset ($q = 1.5\sigma$). Uncertainties correspond to median absolute deviations.

N.B. The calculation of ONC-T parameters (reflectance at *b*, *v* and *x* bands, and *x* band/*b* band ratio) involved NaN values, which were filtered. However, in order to present the results in scatter plots, the NIRS3 parameters (spectral slope, OH band depth, and reflectance at 2.05 µm) were also affected in the process. This led to slightly different median values for NIRS3 parameters, depending on the ONC-T parameter considered. Each subpart of the table represents each case (one for each ONC-T parameter), which is labeled in bold in its upper left cell.

The correlation between the spectral properties of Ryugu in the near-infrared and those in the visible was also investigated at a more local scale. We considered again the large depression in the Northern hemisphere. The results are presented in Table 4.

b band	Class 1	Class 2	Class 3	Class 4	Class 5

NIR spectral slope (%/100 nm)	1.4547 ± 0.2951	2.3088 ± 0.2180	2.8010 ± 0.2050	3.4295 ± 0.2816	0.9084 ± 0.1761
2.72 µm band depth (%)	8.4869 ± 1.0280	9.1229 ± 0.9641	9.4369 ± 0.7353	9.7362 ± 0.9163	7.8999 ± 0.5676
Reflectance at 2.05 µm	0.01856 ± 0.00140	0.01711 ± 0.00132	0.01764 ± 0.00126	0.01798 ± 0.00117	0.01933 ± 0.00175
Reflectance at b band	0.04111 ± 0.00153	0.04114 ± 0.00115	0.04114 ± 0.00128	0.04114 ± 0.00221	0.04100 ± 0.00055

v band	Class 1	Class 2	Class 3	Class 4	Class 5
NIR spectral slope (%/100 nm)	1.4554 ± 0.2960	2.3096 ± 0.2212	2.8170 ± 0.2135	3.3861 ± 0.2626	0.9084 ± 0.1761
2.72 µm band depth (%)	8.4900 ± 1.0333	9.1061 ± 0.9632	9.5417 ± 0.7519	9.2102 ± 0.9119	7.8999 ± 0.5676
Reflectance at 2.05 µm	0.01854 ± 0.00140	0.01712 ± 0.00136	0.01770 ± 0.00125	0.01774 ± 0.00117	0.01933 ± 0.00175
Reflectance at v band	0.04093 ± 0.00093	0.04093 ± 0.00059	0.04114 ± 0.00051	0.04067 ± 0.00119	0.04064 ± 0.00054

x band	Class 1	Class 2	Class 3	Class 4	Class 5
NIR spectral slope (%/100 nm)	1.4550 ± 0.2963	2.3088 ± 0.2215	2.8170 ± 0.2135	3.3861 ± 0.2626	0.9084 ± 0.1761
2.72 µm band depth (%)	8.4855 ± 1.0331	9.0893 ± 0.9577	9.5417 ± 0.7519	9.2102 ± 0.9119	7.8999 ± 0.5676

Reflectance at 2.05 µm	0.01854 ± 0.00140	0.01713 ± 0.00136	0.01770 ± 0.00125	0.01774 ± 0.00117	0.01933 ± 0.00175
Reflectance at x band	0.04085 ± 0.00055	0.04085 ± 0.00037	0.04085 ± 0.00023	0.04085 ± 0.00054	0.04059 ± 0.00034

x/b-band ratio	Class 1	Class 2	Class 3	Class 4	Class 5
NIR spectral slope (%/100 nm)	1.4547 ± 0.2951	2.3088 ± 0.2180	2.8010 ± 0.2050	3.4295 ± 0.2816	0.9084 ± 0.1761
2.72 µm band depth (%)	8.4869 ± 1.0280	9.1229 ± 0.9641	9.4369 ± 0.7353	9.7362 ± 0.9163	7.8999 ± 0.5676
Reflectance at 2.05 µm	0.01856 ± 0.00140	0.01711 ± 0.00132	0.01764 ± 0.00126	0.01798 ± 0.00117	0.01933 ± 0.00175
x band/b band ratio	0.9970 ± 0.0357	0.9963 ± 0.0286	0.9929 ± 0.0324	0.9911 ± 0.0593	0.9864 ± 0.0160

Table 4. Median values of each parameter for each G-mode class obtained with the merged dataset restricted to the area of the large depression (20° < latitude < 60°, 230° < longitude < 300°) ($q = 1.5\sigma$). Uncertainties correspond to median absolute deviations.

Both analyses (at global and local scales) show there is no obvious correlation to the uncertainties considered (see Appendix C. for the correlation coefficients). In particular, the spectral parameter 'ratio *x* band over *b* band' appears invariant for all G-mode classes and very close to unity. This parameter is linked to the spectral slope in the visible spectral range, i.e. between 479.8 nm and 857.3 nm. Thus, regardless of the spectral properties of Ryugu in the near-infrared, the surface seems spectrally flat in the visible. This is in agreement with previous ground-based spectral investigations of Ryugu (e.g. [Perna et al., 2017a]). [Moskovitz

et al., 2013] also noticed that the spectra become redder in the near-infrared spectral range, supporting the latter results obtained *in-situ*. Finally, the analysis of ONC-T data using G-mode in [Barucci et al., 2019] supports the results of our comparison. Indeed, the geographic distribution of the six groups identified for $q = 2.0\sigma$ is fairly different from the one obtained with the NIRS3 data, in particular in the region of the large depression: the surroundings of the depression are assigned to class 1 (mean of Ryugu spectra), thus present no particular spectral properties in the visible, whereas they are clearly redder in the near-infrared (see Figures 5 and 7).

[Domingue et al., 2021] also compared NIRS3 and ONC-T data to determine the regolith properties, using NIRS3 spectra obtained at both near opposition and under opposition. However, they demonstrated the phase reddening on Ryugu is three orders of magnitude greater in the visible than in the near-infrared. Therefore, comparing ONC-T spectra taken under opposition and NIRS3 spectra acquired at phase angles of 30° is reasonable and our comparison remains valid.

5. Conclusion and perspectives

In this work, we selected five thermally and photometrically corrected NIRS3 datasets which maximize the spatial resolution of each region of the surface of Ryugu while ensuring a global coverage. Following the method of [Barucci et al., 2019], we applied the G-mode statistical analysis, first at global scale on the merged dataset, then at local scale on a subset restricted to the intriguing large depression of the Northern hemisphere centered at 50°N, 265°E. The results proved to be consistent at both scales between each other and with the ones obtained by [Barucci et al., 2019]. Spectrally bluer heterogeneities are found notably in the smooth plains of the large depression of the Northern hemisphere. These bluer heterogeneities are also identified by [Matsuoka et al., 2020] with an independent statistical method involving K-

means clustering and Principal Component Analysis, at similar locations, yet in more widespread areas. Nevertheless, the consistency between the results is very encouraging and demonstrated our approach is robust in addition to the higher spatial resolution of the data.

Among other areas, but except the large depression, the floor of all the main craters is spectrally redder than their surroundings, which can be interpreted as the presence of fresher/less weathered material, material with smaller grain size or metamorphism due to shock [Tatsumi et al., 2020b]. The large depression centered at 50°N, 265°E is a particular case: it contains bluer heterogeneities in its interior and is surrounded by redder material from its South to its East. We suggested that the inside of the depression could be more packed than its surroundings, which could explain its smooth aspect, even if a difference of alteration and/or content in fresher material remains more probable. The latter hypothesis could indicate the large depression is older than its surroundings, and its interior has been subsequently covered by bluer regolith coming from further north regions. A comparison between the spectral properties in the near-infrared from the NIRS3 data and in the visible from ONC-T data taken at opposition, using selected spectral parameters, did not reveal any obvious correlation, even with an analysis restricted to the large depression. This also corroborates the results of [Barucci et al., 2019], who applied the Gmode G-mode statistical analysis on ONC-T data using the seven filters available.

Further work is currently ongoing for the analysis of NIRS3 data acquired during the descent phases of the mission. These lower altitude spectra, hence with a very high spatial resolution (tens of centimeters per footprint or better) need more processing, especially a finer thermal correction due to the higher proximity with the surface of Ryugu. The analysis of these very high resolution data will help to derive the fine-scale spectral properties of the surface, hence to put in a wider context the analysis of the returned samples.

Acknowledgements

We thank the Hayabusa2 JAXA team for their efforts in making the mission successful. Hayabusa2 was developed and built under the leadership of JAXA, with contributions from the DLR and the CNES, and in collaboration with NASA, Nagoya University, University of Tokyo, National Astronomical Observatory of Japan, Aizu University, Kobe University, and other universities, institutes, and companies in Japan. We would also like to thank all the engineers who contributed to the success of the Hayabusa2 mission, especially T. Masuda, S. Yasuda, K. Matsushima, and T. Ohshima. We acknowledge financial support from ASI contract No. 2018-27-HH.0 “Partecipazione alla fase E della Missione Hayabusa2”. ED and JDPD thanks the financial support of the Agenzia Spaziale Italiana (ASI, contract No. 2017-37-H.0 CUP F82F17000630005). MA Barucci and M Fulchignoni acknowledge financial support by CNES. The authors are grateful to Eri Tatsumi for having kindly provided the Ryugu map in background of every figure showing the geographic distribution of a G-mode classification, and to Yasuhiro Yokota for having shared the normal albedo map used for the comparison of NIRS3 data with ONC-T data.

Appendices

A. Variables weights of G-mode classifications

For each run of the G-mode, the variables weights are computed. These parameters describe the importance of each variable in the classification, thus which variables drive the most the classification. They are reported in Table A.1.

Wavelength	Global scale	Global scale	Local scale	Local scale

(nm)	$q = 3\sigma$	$q = 1.5\sigma$	$q = 2\sigma$	$q = 1.5\sigma$
1928.7	0.0014	0.0027	0.0029	0.0010
2055.8	0.0017	0.0017	0.0036	0.0025
2182.4	0.0109	0.0056	0.0083	0.0059
2308.5	0.0316	0.0158	0.0212	0.0184
2434.2	0.0448	0.0306	0.0556	0.0345
2559.4	0.0510	0.0614	0.0603	0.0859
2612.8	0.0512	0.0667	0.0675	0.0741
2630.7	0.0513	0.0695	0.0672	0.0953
2648.5	0.0514	0.0595	0.0645	0.0649
2666.3	0.0536	0.0623	0.0538	0.0592
2684.0	0.0509	0.0576	0.0584	0.0499
2701.8	0.0515	0.0450	0.0434	0.0500
2719.6	0.0495	0.0453	0.0388	0.0335
2737.3	0.0482	0.0540	0.0477	0.0451
2755.1	0.0505	0.0672	0.0531	0.0613
2772.8	0.0484	0.0601	0.0574	0.0620
2790.5	0.0502	0.0595	0.0424	0.0446
2808.2	0.0470	0.0400	0.0437	0.0375

2825.9	0.0465	0.0452	0.0449	0.0331
2843.6	0.0465	0.0379	0.0417	0.0378
2861.3	0.0450	0.0281	0.0323	0.0258
2879.0	0.0434	0.0379	0.0352	0.0279
2896.7	0.0315	0.0135	0.0239	0.0181
2914.3	0.0421	0.0328	0.0322	0.0319

Table A.1. Variables weights for the four G-mode classifications presented in this paper.

For the four classifications exposed in this work, the weights are fairly equally distributed for the wavelengths greater than 2.4 µm.

B. Correlation between G-mode classifications and incidence/emission angles

To check for any potential influence of geometric conditions (incidence and emission angles) on the classification obtained using the G-mode, we plotted the incidence angle map (see Figure B.1.) and the emission angle map (see Figure B.2.) of the merged dataset, and the histogram distributions of these two parameters for each G-mode class with $q = 1.5\sigma$ (see Figures B.3. and B.4.).

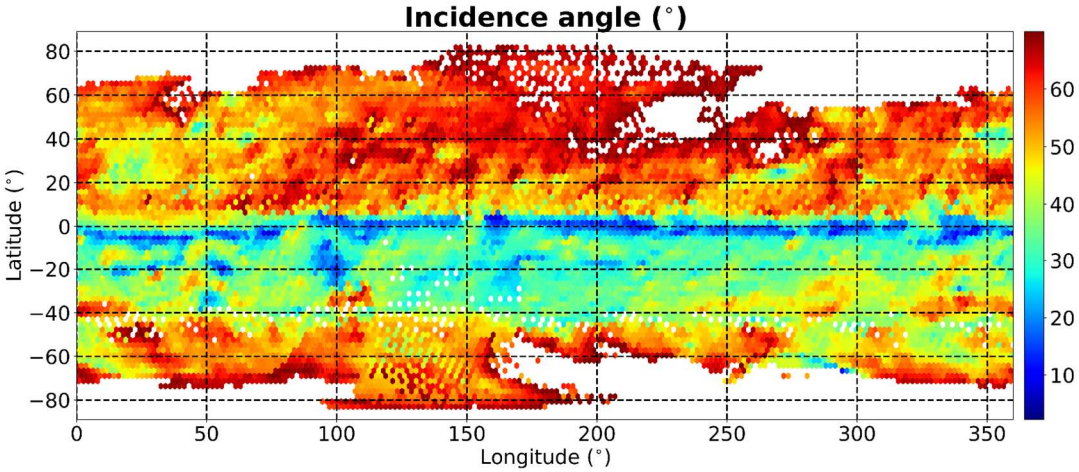

Figure B.1. Incidence angle map of the merged dataset

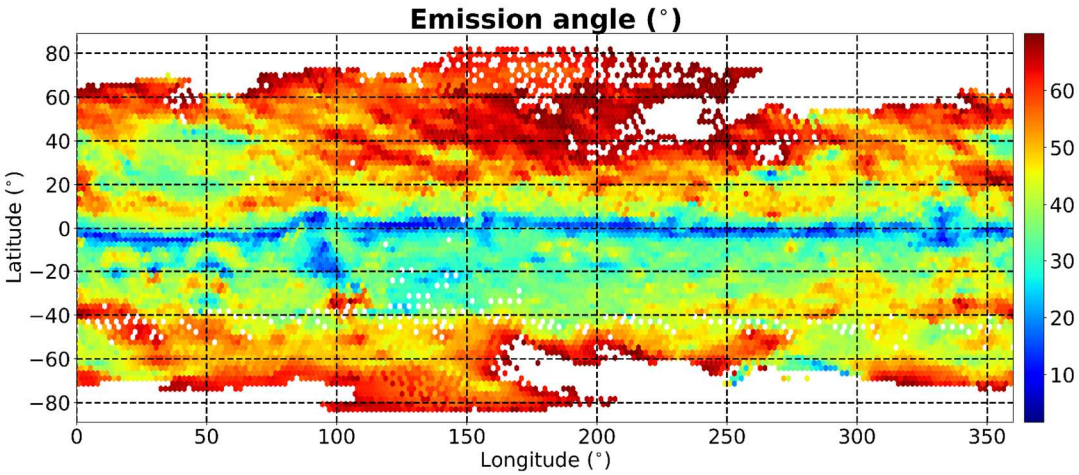

Figure B.2. Emission angle map of the merged dataset

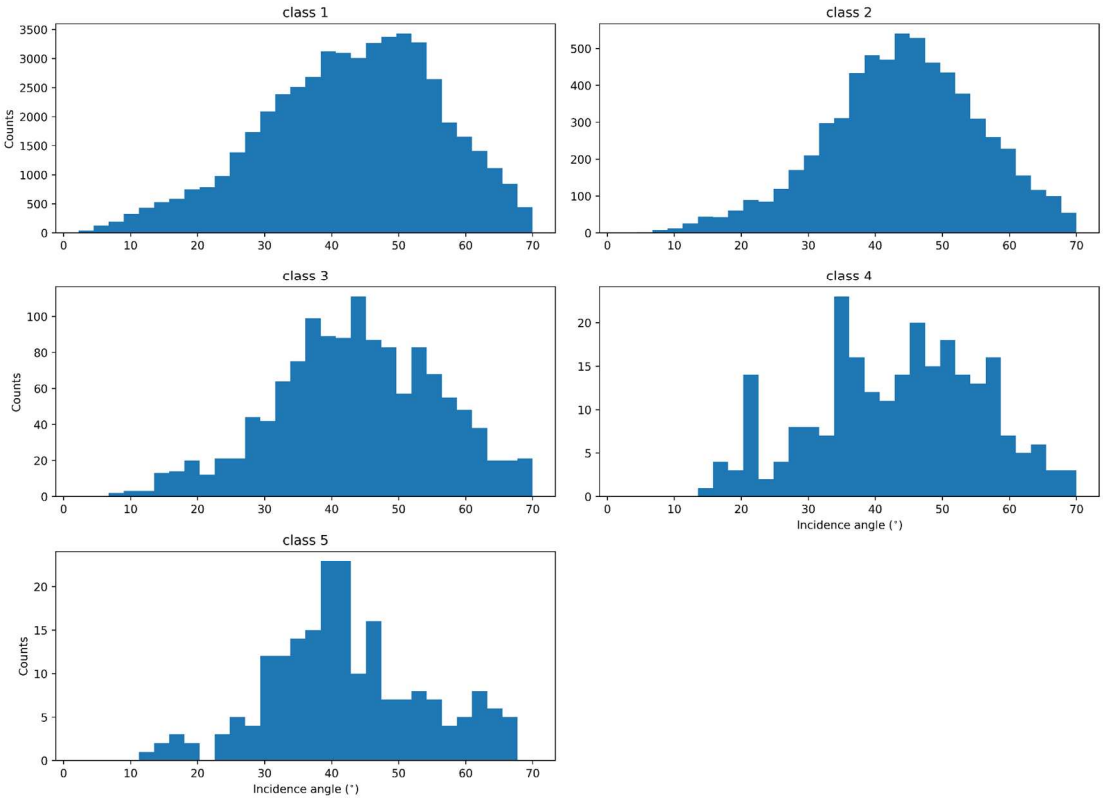

Figure B.3. Histogram distributions of incidence angle for each G-mode class ($q = 1.5\sigma$)

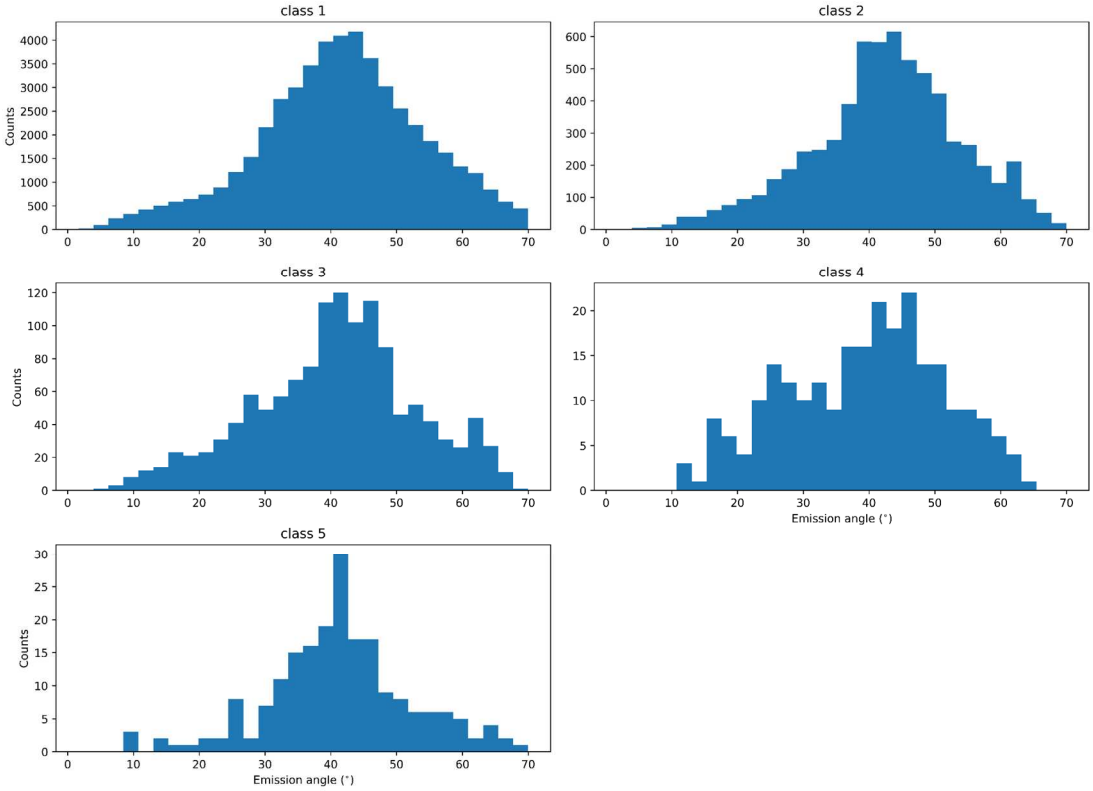

Figure B.4. Histogram distributions of emission angle for each G-mode class ($q = 1.5\sigma$)

Both maps clearly show that the higher the latitude, the higher the incidence and emission angle, which is not the trend observed with the G-mode classification. Histogram distributions do not indicate obvious correlations between the geometric conditions of data acquisition and the resulting G-mode classification.

C. Correlation between NIRS3 spectral parameters and ONC-T spectral parameters

In addition to the scatter plots shown in Section 4, we determined the Pearson correlation coefficients between the three NIRS3 spectral parameters and the four ONC-T spectral parameters. The values are exposed in Tables C.1 (global scale) and C.2 (local scale).

		Reflectance at b band	Reflectance at v band	Reflectance at x band	x band/b band ratio
NIR spectral slope	Class 1	-0.031	-0.095	0.002	0.016
	Class 2	0.027	0.046	-0.029	-0.041
	Class 3	0.037	0.083	-0.001	-0.017
	Class 4	0.182	0.033	0.166	-0.166
	Class 5	-0.033	0.141	0.072	0.055
2.72 µm band depth	Class 1	0.007	-0.013	0.006	-0.011
	Class 2	0.001	-0.006	-0.042	-0.017
	Class 3	0.096	0.051	0.015	-0.091
	Class 4	0.148	0.149	0.033	-0.094
	Class 5	0.087	-0.084	0.149	-0.055
Reflectance at 2.05 µm	Class 1	-0.007	-0.089	0.013	-0.028
	Class 2	-0.197	-0.211	-0.132	0.141
	Class 3	-0.205	-0.230	-0.167	0.165
	Class 4	-0.071	-0.212	-0.195	0.012
	Class 5	0.071	0.070	0.069	-0.083

Table C.1. Pearson correlation coefficients between NIRS3 spectral parameters and ONC-T spectral parameters at global scale. Each G-mode class case is considered separately.

		Reflectance at b band	Reflectance at v band	Reflectance at x band	x band/b band ratio
NIR spectral slope	Class 1	-0.041	-0.022	0.012	0.053
	Class 2	-0.015	-0.011	-0.104	-0.008
	Class 3	0.109	0.217	0.107	-0.096
	Class 4	-0.328	-0.260	-0.271	0.289
	Class 5	-0.069	-0.142	0.341	0.258
2.72 µm band depth	Class 1	0.062	0.055	0.063	-0.049
	Class 2	0.045	0.116	0.046	-0.044
	Class 3	0.119	0.024	0.104	-0.107
	Class 4	0.506	0.476	0.353	-0.460
	Class 5	0.238	0.016	0.102	-0.235
Reflectance at 2.05 µm	Class 1	0.018	0.013	0.019	-0.025
	Class 2	-0.005	-0.008	0.019	0.021
	Class 3	0.257	0.224	-0.024	-0.276
	Class 4	0.552	0.578	0.561	-0.482
	Class 5	0.005	0.486	-0.660	-0.323

Table C.2. Pearson correlation coefficients between NIRS3 spectral parameters and ONC-T spectral parameters at local scale. Each G-mode class case is considered separately.

All correlation coefficients are low at global scale ($|r_P|<0.23$). The majority of correlation coefficients are also low at local scale, although some are moderate ($|r_P|<0.66$). This confirms the absence of obvious correlation between NIRS3 spectral parameters and ONC-T spectral parameters stated in Section 4.

References

Barucci, M. A., et al., 1987, Classification of asteroids using G-mode analysis, *Icarus*, Volume 72, Issue 2, p. 304-324. DOI: 10.1016/0019-1035(87)90177-1

Barucci, M. A., et al., 2005, Taxonomy of Centaurs and Trans-Neptunian Objects, *The Astronomical Journal*, Volume 130, Issue 3, pp. 1291-1298. DOI: 10.1086/431957

Barucci, M. A., et al., 2019, Multivariable statistical analysis of spectrophotometry and spectra of (162173) Ryugu as observed by JAXA Hayabusa2 mission, *Astronomy & Astrophysics*, Volume 629, id.A13, 10 pp. DOI: 10.1051/0004-6361/201935851

Barucci, M. A., et al., 2020, OSIRIS-REx spectral analysis of (101955) Bennu by multivariate statistics, *Astronomy & Astrophysics*, Volume 637, id.L4, 5 pp. DOI: 10.1051/0004-6361/202038144

Binzel, R. P., et al., 2015, Spectral slope variations for OSIRIS-REx target Asteroid (101955) Bennu: Possible evidence for a fine-grained regolith equatorial ridge, *Icarus*, Volume 256, p. 22-29. DOI: 10.1016/j.icarus.2015.04.011

Coradini, A., et al., 1977, A FORTRAN V program for a new classification technique: the g-mode central method, *Computers & Geosciences*, Volume 3, Issue 1, pp. 85-105. DOI: 10.1016/0098-3004(77)90035-8

Cloutis, E. A., et al., 2018, Spectral reflectance "deconstruction" of the Murchison CM2 carbonaceous chondrite and implications for spectroscopic investigations of dark asteroids, *Icarus*, Volume 305, p. 203-224. DOI: 10.1016/j.icarus.2018.01.015

Domingue, D., et al., 2021, Spectrophotometric Properties of 162173 Ryugu's Surface from the NIRS3 Opposition Observations, *The Planetary Science Journal*, Volume 2, Issue 5, id.178, 22 pp. DOI: 10.3847/PSJ/ac14bb

Fulchignoni, M., et al., 2000, The Extension of the G-Mode Asteroid Taxonomy, *Icarus*, Volume 146, Issue 1, pp. 204-212. DOI: 10.1006/icar.2000.6381

Gavrishin, A. I., et al., 1992, Multivariate Classification Methods in Planetary Sciences, *Earth, Moon and Planets*, Volume 59, Issue 2, pp.141-152. DOI: 10.1007/BF00058728

Hasselmann, P. H., et al., 2013, Adapted G-mode Clustering Method applied to Asteroid Taxonomy, *Proceedings of the 12th Python in Science Conference (SciPy 2013)*, p. 48-55.

Iwata, T., et al., 2017, NIRS3: The Near Infrared Spectrometer on Hayabusa2, *Space Science Reviews*, Volume 208, Issue 1-4, pp. 317-337. DOI: 10.1007/s11214-017-0341-0

Kameda, S., et al., 2017, Preflight Calibration Test Results for Optical Navigation Camera Telescope (ONC-T) Onboard the Hayabusa2 Spacecraft, *Space Science Reviews*, Volume 208, Issue 1-4, pp. 17-31. DOI: 10.1007/s11214-015-0227-y

Kitazato, K., et al., 2019, The surface composition of asteroid 162173 Ryugu from Hayabusa2 near-infrared spectroscopy, *Science*, Volume 364, Issue 6437, pp. 272-275. DOI: 10.1126/science.aav7432

Lantz, C., et al., 2017, Ion irradiation of carbonaceous chondrites: A new view of space weathering on primitive asteroids, *Icarus*, Volume 285, p. 43-57. DOI: 10.1016/j.icarus.2016.12.019

Matsuoka, M., et al., 2020, Clustering Analysis of NIRS3 Infrared Spectral Data of Ryugu, *51st Lunar and Planetary Science Conference*, id.1724.

Moskovitz, N. A., et al., 2013, Rotational characterization of Hayabusa II target Asteroid (162173) 1999 JU3, *Icarus*, Volume 224, Issue 1, pp. 24-31. DOI: 10.1016/j.icarus.2013.02.009

Perna, D., et al., 2017a, Spectral and rotational properties of near-Earth asteroid (162173) Ryugu, target of the Hayabusa2 sample return mission, *Astronomy & Astrophysics*, Volume 599, L1. DOI: 10.1051/0004-6361/201630346

Perna, D., et al., 2017b, Multivariate statistical analysis of OSIRIS/Rosetta spectrophotometric data of comet 67P/Churyumov-Gerasimenko, *Astronomy & Astrophysics*, Volume 600, id.A115, 9 pp. DOI: 10.1051/0004-6361/201630015

Pilorget, C., et al., 2021, First compositional analysis of Ryugu samples by the MicrOmega hyperspectral microscope, *Nature Astronomy,* Advanced Online Publication. DOI: 10.1038/s41550-021-01549-z

Sugita, S., et al., 2019, The geomorphology, color, and thermal properties of Ryugu: Implications for parent-body processes, *Science*, Volume 364, Issue 6437, id. eaaw0422. DOI: 10.1126/science.aaw0422

Suzuki, H., et al., 2018, Initial inflight calibration for Hayabusa2 optical navigation camera (ONC) for science observations of asteroid Ryugu, *Icarus*, Volume 300, pp. 341-359. DOI: 10.1016/j.icarus.2017.09.011

Tachibana, S., et al., 2022, Pebbles and sand on asteroid (162173) Ryugu: In situ observation and particles returned to Earth, *Science*, Volume 375, Issue 6584, pp. 1011-1016. DOI: 10.1126/science.abj8624

Tatsumi, E., et al., 2020a, Global photometric properties of (162173) Ryugu, *Astronomy & Astrophysics*, Volume 639, id.A83, 19 pp. DOI: 10.1051/0004-6361/201937096

Tatsumi, E., et al., 2020b, Visible color of the artificial crater on Ryugu created by Small Carry-on Impactor, *14th Europlanet Science Congress 2020*, id. EPSC2020-331. DOI: 10.5194/epsc2020-331

Tatsumi, E., et al., 2021, Spectrally blue hydrated parent body of asteroid (162173) Ryugu, *Nature Communications*, Volume 12, article id. 5837. DOI: 10.1038/s41467-021-26071-8

Tosi, F., et al., 2005, G-Mode Classification of Spectroscopic Data, *Earth, Moon, and Planets*, Volume 96, Issue 3-4, pp. 165-197. DOI: 10.1007/s11038-005-9061-7

Watanabe, S., et al., 2017, Hayabusa2 Mission Overview, *Space Science Reviews*, Volume 208, Issue 1-4, pp. 3-16. DOI: 10.1007/s11214-017-0377-1

Watanabe, S., et al., 2019, Hayabusa2 arrives at the carbonaceous asteroid 162173 Ryugu - A spinning top-shaped rubble pile, *Science*, Volume 364, Issue 6437, pp. 268-272. DOI: 10.1126/science.aav8032

Yada, T., et al., 2021, Preliminary analysis of the Hayabusa2 samples returned from C-type asteroid Ryugu, *Nature Astronomy*, Advanced Online Publication. DOI: 10.1038/s41550-021-01550-6

Yokota, Y., et al., 2021, Opposition Observations of 162173 Ryugu: Normal Albedo Map Highlights Variations in Regolith Characteristics, *The Planetary Science Journal*, Volume 2, Issue 5, id.177, 32 pp. DOI: 10.3847/PSJ/ac14ba

Young, E. D., et al., 2022, The Oxygen Isotopic Composition of Samples Returned from Asteroid Ryugu: Evidence for Similarity to CI Chondrites, *53rd Lunar and Planetary Science Conference*, id.1290